

Evolution mapping II: describing statistics of the non-linear cosmic velocity field.

Matteo Esposito¹★, Ariel G. Sánchez¹, Julien Bel², and Andrés N. Ruiz^{3,4}

¹Max-Planck-Institut für Extraterrestrische Physik, Postfach 1312, Giessenbachstr., D-85748 Garching, Germany

²Aix Marseille Univ, Université de Toulon, CNRS, CPT, Marseille, France

³Instituto de Astronomía Teórica y Experimental (CONICET-UNC), Laprida 854, X5000BGR, Córdoba, Argentina

⁴Observatorio Astronómico, Universidad Nacional de Córdoba, Laprida 854, X5000BGR, Córdoba, Argentina

Accepted XXX. Received YYY; in original form ZZZ

ABSTRACT

We extend the evolution mapping approach, introduced in the first paper of this series to describe non-linear matter density fluctuations, to statistics of the cosmic velocity field. This framework classifies cosmological parameters into shape parameters, which determine the shape of the linear matter power spectrum, $P_L(k, z)$, and evolution parameters, which control its amplitude at any redshift. Evolution mapping leverages the fact that density fluctuations in cosmologies with identical shape parameters but different evolution parameters exhibit similar non-linear evolutions when expressed as a function of clustering amplitude. We analyse a suite of N-body simulations sharing identical shape parameters but spanning a wide range of evolution parameters. Using a method for estimating the volume-weighted velocity field based on the Voronoi tessellation of simulation particles, we study the non-linear evolution of the velocity divergence power spectrum, $P_{\theta\theta}(k)$, and its cross-power spectrum with the density field, $P_{\delta\theta}(k)$. We demonstrate that the evolution mapping relation applies accurately to $P_{\theta\theta}(k)$ and $P_{\delta\theta}(k)$. While this breaks down in the strongly non-linear regime, deviations can be modelled in terms of differences in the suppression factor, $g(a) = D(a)/a$, similar to those for the density field. Such modelling describes the differences in $P_{\theta\theta}(k)$ between models with the same linear clustering amplitude to better than 1 percent accuracy at all scales and redshifts considered. Evolution mapping simplifies the description of the cosmological dependence of non-linear density and velocity statistics, streamlining the sampling of large cosmological parameter spaces for cosmological analysis.

Key words: cosmology: cosmological parameters — cosmology: large-scale structure of the Universe — cosmology: theory — methods: numerical — software: simulations

1 INTRODUCTION

The emergence of organised cosmic structures has been an important focus for cosmologists since the advent of large-scale surveys. The millions of observed galaxies reveal an intricate network of filaments and clusters that we call *cosmic web* (Peebles 1980). Observations of such clustering of galaxies can provide insights into fundamental physics and offer a way to test our understanding of gravity and of the components that make up our Universe (see e.g., Efstathiou et al. 2002; Eisenstein et al. 2005; Cole et al. 2005; Alam et al. 2017; Alam et al. 2021; DESI Collaboration et al. 2024). However, this can only be achieved if such impressive galaxy clustering surveys are accompanied by comparable theoretical models and techniques.

N-body simulations are the ideal tool for detailed studies of non-linear structure formation (Efstathiou et al. 1985; Kravtsov et al. 1997; Teyssier 2002; Springel 2005; Springel et al. 2021; Potter et al. 2017; Garrison et al. 2019). By numerically solving the equations of motion for a large number of particles, these simulations can

model the evolution of cosmic structures from the early universe to the present day. N-body simulations are crucial for testing theoretical models against observational data, as they can account for nonlinear gravitational effects that are difficult to capture analytically. However, such accurate simulations come at the cost of high computational complexity. Large suites of simulations are often needed to explore different cosmologies, requiring numerous CPU hours on high-performance computer clusters. For this reason, exploiting our understanding of cosmology is paramount to aiding the exploration of wide cosmological parameter spaces.

With this in mind, Sánchez et al. (2022) pointed out that a useful degeneracy is revealed if one classifies cosmological parameters into two groups: shape parameters, Θ_s , which determine the shape of the linear matter power spectrum, $P_L(k, z)$, and evolution parameters, Θ_e , which only affect its amplitude at any given redshift. With this definition, the time evolution of $P_L(k, z)$ in models sharing the same shape parameters but different evolution parameters can be mapped from one to the other by relabelling the redshifts that correspond to the same linear clustering amplitude. This *evolution mapping* relation not only simplifies comparing different cosmological models but also

★ esposito@mpe.mpg.de

accurately describes the non-linear matter power spectrum of the full density field (Sánchez et al. 2022).

However, the density field cannot be observed directly. In particular, galaxy positions along the line of sight can only be inferred from their redshift, which is also influenced by the galaxies’ peculiar velocities (Kaiser 1987). The modelling of this effect—the so-called redshift-space distortions (RSD)—is fundamental for producing accurate predictions of the observational data. Moreover, these velocities arise from gravitational interactions within the large-scale structure, providing additional information about the underlying mass distribution and the dynamics of cosmic structures (Guzzo et al. 2008). For this reason, this paper aims to use evolution mapping to simplify the modelling of velocity statistics.

To achieve this, we employ the *Aletheia* simulations. These simulations share the same shape parameters but adopt different evolution parameters. For each simulation, we analyze snapshots at the redshifts at which the different cosmologies have the same amplitude of linear matter perturbations and, thus, also the same linear matter power spectrum. We show in this way how the evolution mapping relation can also be applied to statistics of the velocity field and, in particular, to the auto-power spectrum of the velocity divergence, $P_{\theta\theta}(k)$, and its cross-power spectrum with the density field, $P_{\delta\theta}(k)$. These are two crucial ingredients in semi-analytical recipes for RSD (Scoccimarro 2004).

Estimating the velocity field in N-body simulations is, however, a complex task: due to the lack of particles in under-dense regions, such portions of the simulation are left with little information. For this reason, different methods have been proposed to reconstruct the velocity field in the voids between particles (see, e.g., Hahn et al. 2015; Bel et al. 2019; Feldbrugge 2024, for recent implementations). In this work, we employ a modification of an algorithm based on the approximation that the velocity field is constant in the cells of the Voronoi tessellation of the N-body tracers (Bernardeau & van de Weygaert 1996).

Equipped with simulations that span a wide range of evolution parameters and an algorithm to accurately and efficiently reconstruct the velocity field, we show how the evolution mapping relation can also be applied to $P_{\theta\theta}(k)$ and $P_{\delta\theta}(k)$. We demonstrate how the small deviations we find from the perfect mapping can be attributed to differences in the growth of structure histories of the different models and can be described with the same recipes proposed in Sánchez et al. (2022) as a function of the suppression factor $g(a) = D(a)/a$.

We begin in Section 2 by summarising the results of Sánchez et al. (2022) on the matter power spectrum and argue why these should also apply to $P_{\theta\theta}(k)$ and $P_{\delta\theta}(k)$. In Section 3, we present the *Aletheia* simulations, and in Section 4, we describe the method used to estimate the velocity field from them. In Section 5 we present and discuss our results. Finally, we give our conclusions in Section 6. We include in Appendix A a discussion on a problem that emerges when dealing with GADGET-4 simulations if the user is interested in the velocities of snapshots at a very precise redshift.

2 EVOLUTION MAPPING

2.1 The matter power spectrum

One of the successes of the standard Λ CDM model resides in its ability to describe the physics of cosmic structure formation through a relatively small number of parameters. Although different parameter bases are equivalent, choosing one that explicitly exhibits degeneracies in the statistics of interest (in our case, the matter power

spectrum) can simplify its modelling and understanding. With this in mind, we focus on the parameters

$$\Theta = (\omega_\gamma, \omega_b, \omega_c, \omega_{\text{DE}}, \omega_K, w_0, w_a, A_s, n_s). \quad (1)$$

Here, ω_i represents the physical energy densities of radiation (γ), baryons (b), cold dark matter (c), dark energy (DE), and curvature (K), given by

$$\omega_i = \frac{8\pi G}{3H_{100}^2} \rho_i, \quad (2)$$

in terms of their present-day densities ρ_i and $H_{100} = 100 \text{ km s}^{-1} \text{ Mpc}^{-1}$. We allow for a time-dependent dark energy equation-of-state parameter, $w_{\text{DE}}(a)$, described in terms of the linear parametrization (Chevallier & Polarski 2001; Linder 2003)

$$w_{\text{DE}}(a) = w_0 + w_a(1 - a). \quad (3)$$

Finally, the values of A_s and n_s describe the amplitude and spectral index of the primordial power spectrum.

Sánchez et al. (2022) showed that the parameters of equation (1) can be classified in terms of their impact on the linear matter power spectrum, $P_L(k, z)$, into *shape* and *evolution* parameters. The former set includes

$$\Theta_s = (\omega_\gamma, \omega_b, \omega_c, n_s), \quad (4)$$

which determine the shape of the primordial power spectrum and the transfer function. The latter set contains

$$\Theta_e = (\omega_{\text{DE}}, \omega_K, w_0, w_a, A_s), \quad (5)$$

which only affect the amplitude of $P_L(k)$ at any given redshift z . For non-flat cosmologies, the primordial power spectrum deviates from a simple power-law on large scales. Dynamic dark energy models also show scale-dependent features in $P_L(k, z)$ on super-horizon scales. However, the scales at which these effects are significant are larger than the ones considered in this work. Therefore, these parameters can be treated effectively as evolution parameters.

Since changes in the values of the evolution parameters, as well as in the redshift z (through the growth factor), only affect the amplitude of $P_L(k, z)$, they are all degenerate with each other. Therefore, the effects of these parameters can be captured by a single quantity representing the amplitude of $P_L(k, z)$. This is often given in terms of the RMS variance of the linear-theory density field at a reference scale R as

$$\sigma^2(R) = \frac{1}{2\pi^2} \int dk k^2 P_L(k, z) W^2(kR), \quad (6)$$

where $W^2(kR)$ is the Fourier transform of a top-hat window function at a scale R . We follow Sánchez (2020) and adopt $\sigma_{12} := \sigma(R = 12 \text{ Mpc})$ as our parameter for measuring the amplitude of $P_L(k, z)$. With this choice, the evolution parameters will only affect $P_L(k, z)$ through their effect on σ_{12} . In other words, independently of the combination of evolution parameters and redshift, the linear matter power spectra of models with the same shape parameters and σ_{12} will be indistinguishable, that is

$$P_L(k|z, \Theta_s, \Theta_e) = P_L(k|\Theta_s, \sigma_{12}(z, \Theta_s, \Theta_e)). \quad (7)$$

This simple relation exposes how, for a fixed set of shape parameters, $P_L(k, z)$ of cosmologies with different evolution parameters can be mapped to one another by simply relabelling the redshifts that correspond to the same σ_{12} . Following Sánchez et al. (2022), we will hereafter refer to equation (7) as the *evolution mapping* relation.

We explicitly left out the physical density of massive neutrinos,

ω_ν , in equation (4). Massive neutrinos lead to a time-dependent suppression of power at small scales induced by neutrino free-streaming. This means that the growth factor becomes scale-dependent, breaking the evolution-mapping relation. However, it is possible to extend the evolution mapping framework to include cosmologies with $\omega_\nu \neq 0$ by considering a reference cosmology without massive neutrinos and $\omega'_c = \omega_c + \omega_\nu$. We leave a detailed description of this treatment for future work (Finkbeiner et al., in prep.) and focus here only on cosmologies without massive neutrinos.

Note that the degeneracy of equation (7) cannot be described in terms of the traditional parameter $\sigma_{8/h} = \sigma(R = 8 h^{-1} \text{Mpc})$ and that it breaks if the so-called Hubble units, $h^{-1} \text{Mpc}$, are adopted. The dimensionless Hubble parameter $h = H_0/H_{100}$ is given by the sum of all physical density parameters as

$$h^2 = \sum_i \omega_i, \quad (8)$$

and as such, it represents a mixture of shape and evolution parameters. Using quantities that explicitly depend on h , such as $\sigma_{8/h}$ or the *fractional* density parameters $\Omega_i := \omega_i/h^2$, obscures this degeneracy. For this reason, throughout this work, we will provide all results in Mpc units.

The perfect correspondence described by equation (7) is strictly valid only in the linear regime, as non-linear dynamics couples the evolution of different Fourier modes. Nevertheless, since $P_L(k, z)$ plays a dominant role in shaping the non-linear matter power spectrum, the degeneracy outlined in equation (7) largely carries over to the non-linear regime. This effect is especially noticeable in the framework of standard perturbation theory (SPT). If we assume that the perturbation kernels are independent of cosmological parameters—which holds for an Einstein-de-Sitter (EdS) universe and is a reasonable approximation even for non-standard cosmologies (Takahashi 2008; Taruya 2016; Garny & Taule 2021)—SPT predicts that the non-linear power spectrum depends solely on $P_L(k, z)$, without explicit dependence on the cosmological parameters. Sánchez et al. (2022) used N-body simulations of cosmologies sharing the same shape parameters but differing in evolution parameters to show that the matter power spectra measured at redshifts where these cosmologies have the same value of σ_{12} remain extremely similar. This provides an approximate evolution mapping relation

$$P(k|z, \Theta_s, \Theta_e) \sim P(k|\Theta_s, \sigma_{12}(z, \Theta_s, \Theta_e)). \quad (9)$$

Deviations from this mapping are found at small scales and become larger as the non-linear evolution becomes more prominent, i.e. with increasing σ_{12} . Such deviations are due to the different growth histories that the models experience and can be modelled in terms of the suppression factor $g(a) = D(a)/a$ and its derivative $g'(a) = dg/d\sigma_{12}$. Sánchez et al. (2022) proposed a phenomenological recipe for predicting how each model deviates from a reference ΛCDM one by Taylor expanding $P(k)$ around their value of g and g' and using the difference in these quantities to predict the deviations in the $P(k)$ as

$$P(k|g, g') = P(k|g_0, g'_0) + \frac{\partial P}{\partial g}(k|g_0, g'_0) \cdot (g - g_0) + \frac{\partial P}{\partial g'}(k|g_0, g'_0) \cdot (g' - g'_0), \quad (10)$$

where g_0, g'_0 indicate the values at the reference model and all quantities are evaluated at the same Θ_s and σ_{12} .

The ansatz of equation (10) is highly effective at describing the differences in the non-linear matter power spectra of different cosmologies. In the rest of the paper, we will show how evolution map-

ping can also be applied to the cosmic velocity field. In particular, we will focus on modelling the power spectrum of the divergence of the velocity field and its cross-power spectrum with the density field, and show how equation (10) is also effective for predicting these quantities.

2.2 The cosmic velocity field

We will now show that equation (9) can also be applied, with some adjustments, to velocity statistics. Let us start with linear perturbation theory, in which the relation between the density contrast δ and the peculiar velocity field \mathbf{v} of a pressureless fluid is given by the continuity equation (see, e.g., Mo et al. 2010, for a pedagogical derivation)

$$\frac{\partial \delta(\mathbf{x}, t)}{\partial t} + \frac{\nabla \cdot \mathbf{v}(\mathbf{x}, t)}{a} = 0, \quad (11)$$

where t is the cosmic time associated to a comoving observer, \mathbf{x} are the comoving coordinates and $\mathbf{v} := a d\mathbf{x}/dt$ is the peculiar velocity relative to the background expansion. Going to Fourier space, equation (11) can be expressed as

$$\mathbf{i}\mathbf{k} \cdot \frac{\mathbf{v}_{\mathbf{k}}}{af(a)H(a)} = -\delta_{\mathbf{k}}, \quad (12)$$

where the logarithmic growth rate $f(a) := d \ln D(a)/d \ln a$ is the logarithmic derivative of the linear growth factor $D(a)$ with respect to the scale factor a .

Let us now define a rescaled velocity field, $\Upsilon_{\mathbf{k}}$, and its divergence, $\theta_{\mathbf{k}}$, as

$$\Upsilon_{\mathbf{k}} := -\frac{\mathbf{v}_{\mathbf{k}}}{af(a)H(a)}; \quad \theta_{\mathbf{k}} := \mathbf{i}\mathbf{k} \cdot \Upsilon_{\mathbf{k}}. \quad (13)$$

In terms of these quantities, equation (12) can be conveniently expressed as

$$\theta_{\mathbf{k}} = \delta_{\mathbf{k}}, \quad (14)$$

and we can express the relation between the auto and cross-power spectra of $\delta_{\mathbf{k}}$ and $\theta_{\mathbf{k}}$ as

$$P_{\theta\theta}(k) = P_{\delta\delta}(k) = P_{\delta\delta}(k), \quad (15)$$

where $P_{\delta\delta}(k)$ corresponds to the linear-theory matter power spectrum defined above as $P_L(k)$. Hence, if evolution mapping applies to $P_L(k)$, it must also work for the rescaled velocity field $\Upsilon_{\mathbf{k}}$.

It is instructive to show what this rescaled velocity field corresponds to. Let us make a change of variables and use the overall amplitude of clustering as a time variable, or more precisely $\tau := \ln \sigma_{12}$

$$\frac{d\mathbf{x}}{d\tau} = \frac{d\mathbf{x}}{dt} \frac{dt}{d\tau} = \frac{\mathbf{v}(t)}{af(a)H(a)} = -\Upsilon(t). \quad (16)$$

This implies that this rescaled velocity field is obtained with a change of time variable (Nusser & Colberg 1998). In other words, what will be identical at the linear level in cosmologies with the same shape parameters but different evolution parameters and evaluated at the same σ_{12} are not the trajectories in units of t but rather those in units of the clustering amplitude, namely $\ln \sigma_{12}$. In the following, we will always refer to the velocity field and its divergence in units of $\ln \sigma_{12}$.

3 THE ALETHEIA SIMULATIONS

We employed a suite of N-body simulations, the *Aletheia* simulations, to measure how accurately evolution mapping can describe

Parameter	Value	Parameter	Value
ω_b	0.02244	w_0	-1
ω_c	0.1206	w_a	0
ω_{DE}	0.3059	n_s	0.97
ω_K	0	$\sigma_{12}(z=0)$	0.825
h	0.67	A_s	2.127×10^{-9}

Table 1. Cosmological parameters of our reference Λ CDM model. The value of h is obtained from equation (8). The value of A_s is set to match the chosen $\sigma_{12}(z=0)$.

the velocity divergence auto-power spectrum $P_{\theta\theta}(k)$ and its cross-power spectrum with the density field $P_{\delta\theta}(k)$ in the non-linear regime. We performed these simulations with GADGET-4 (Springel et al. 2021) with 1500^3 particles and a box side length of 1492.5 Mpc ($1000 h^{-1}$ Mpc). The suite spans nine different cosmologies that share the same shape parameters but differ in their evolution parameters. The reference model is a Λ CDM universe with Planck-like values for the cosmological parameters, shown in Table 1. In the rest of the models, we vary around the reference values ω_{DE} , w_0 , w_a and ω_K . We also include a model with an Einstein-de Sitter (EdS) cosmology for which $\omega_{DE} = 0$. For each model that varies a density parameter (either ω_{DE} or ω_K), we compensate with a change of h or ω_{DE} . Each model has a fixed $\sigma_{12}(z=0) = 0.825$. Hence, the values of A_s in the different models are adjusted to reach the given overall amplitude of $P_L(k, z)$. A summary of the parameters for each cosmology is shown in Table 2.

We obtained two realizations for each simulation following the paired-fixed recipe of Angulo & Pontzen (2016) to suppress cosmic variance. We generated the initial conditions (ICs) for the simulations with 2LPTIC (Crocce et al. 2006). To minimise the variance introduced by the generation of the ICs, we generated only one pair of boxes and varied the starting redshift for each simulation to match the σ_{12} of the given box. This is allowed because at the same σ_{12} and at the linear level, all these cosmologies exhibit the same density distribution. Although the same is not true for the velocity field, as shown in equation (16), it is valid for the rescaled velocity Y . Hence, for each cosmology, we rescaled the velocities from the reference ICs by the ratios of the corresponding factors $af(a)H(a)$. Finally, given that GADGET-4 takes the ICs in Hubble units as input, we also rescaled the positions and box sizes for the models with different values of h .

We produced five snapshots for each model at the redshifts at which each cosmology reaches a given value of σ_{12} . This means that our snapshots are at the same σ_{12} rather than at the same redshift, and thus, all these snapshots have the same $P_L(k, z)$ (and consequently also identical linear-theory $P_{\theta\theta}(k, z)$, $P_{\delta\theta}(k, z)$, equation (15)).

The simulations in this work replicate the ones employed in Sánchez et al. (2022), with some differences. First, we replaced the Early Dark Energy (EdE) model with the EdS one. This choice comes from the fact that the EdE simulation was performed with an effective model that only considered the impact of EdE on the Hubble function and the growth factor. More generally, EdE models can also change the shape of the transfer function. Thus, we decided to substitute that model with an EdS cosmology, which is often used as a baseline for theoretical modelling and will be useful for future applications. Secondly, the simulations of Sánchez et al. (2022) were performed starting from fixed redshift rather than fixed σ_{12} as described above.

Finally, the most important change resides in the way the GADGET-4 snapshots are produced. In particular, the simulations in (Sánchez et al. 2022) were performed with a compile-time option (OUT-

PUT_NONSYNCHRONIZED_ALLOWED) to address a limitation in how GADGET-4 produces snapshots. As GADGET-4 uses an adaptive time-stepping scheme, it synchronizes particles only at specific times, known as *synchronization points*. This means particles in different regions of the simulation (dense or underdense) are updated at different rates based on their local conditions. As a result, particles are only synchronized at these designated points. When the user requests a snapshot at a given redshift, GADGET-4’s default behaviour is to save it at the closest available *synchronization point*. This may result in small shifts in redshift, undesirable in our analysis in which we want to compare simulations at the exact same value of σ_{12} . The OUTPUT_NONSYNCHRONIZED_ALLOWED option allows GADGET-4 to output snapshots at the exact redshift requested by linearly drifting particle positions to the desired time. However, while the positions are adjusted to the correct redshift, the particle velocities are left unchanged, meaning they correspond to different times. As a result, the snapshot contains inconsistent velocities at different redshifts, which can introduce errors in velocity-related analyses.

To address this problem while ensuring that the snapshots are exactly at the desired redshifts, we performed this new set of simulations with a *start-stop* method. This method leverages the fact that all particles are naturally synchronized at the start and end of each simulation run. By stopping the simulation at each required snapshot and restarting it with adjusted start and end times, we ensure that all particles are fully synchronized at the exact redshift requested. This guarantees consistent outputs for both positions and velocities. Readers interested in a more detailed discussion of the problem can find it in Appendix A, along with tests of the *start-stop* method.

4 ESTIMATING THE DENSITY AND VELOCITY POWER SPECTRA

Estimating velocity statistics in N-body simulations (and for similar reasons in observations) is intrinsically difficult because particles trace the density field and not the velocity one. The lack of particles in underdense regions is indicative of their density but can give little to no information on the velocity field inside them. Low-density regions suffer from large Poisson errors and in regions where there are no particles at all the velocity field remains completely undetermined (see, e.g. Juszkiewicz et al. 1995; Bernardeau & van de Weygaert 1996; Bernardeau et al. 1997). For this reason, different techniques have been developed for recovering the volume-weighted velocity field from N-body simulations (van de Weygaert & Bernardeau 1998; Romano-Díaz & van de Weygaert 2007; Pueblas & Scoccimarro 2009; Jennings et al. 2011; Jennings 2012; Jennings et al. 2015; Zheng et al. 2013; Koda et al. 2014; Zheng et al. 2015; Zhang et al. 2015; Yu et al. 2015; Bel et al. 2019). A common choice is to employ the Delaunay tessellation field estimator algorithm (DTFE, Schaap & van de Weygaert 2000; Cautun & van de Weygaert 2011), in which the Delaunay tessellation¹ of the N-body particles is used to interpolate the velocity to every point in space under the assumption that the field is continuous and with a constant gradient inside each tetrahedra. This results in a volume-weighted estimate of the velocity field instead of the mass-weighted outcome obtained using standard particle-in-cell techniques.

In this work, we follow a different approach based on the work of Bernardeau & van de Weygaert (1996), that implies a lower-order

¹ In a Delaunay tessellation, particles are linked to each other, forming a set of tetrahedra such that no particle is inside the circumsphere of any tetrahedron, optimizing for tetrahedra to be as close to equiangular as possible.

Model	Definition	Redshifts of snapshots at given σ_{12}					
		z_{IC}	$\sigma_{12} = 0.343$	$\sigma_{12} = 0.499$	$\sigma_{12} = 0.611$	$\sigma_{12} = 0.703$	$\sigma_{12} = 0.825$
Model 0	Reference Λ CDM (Table 1)	99.0	2.000	1.000	0.570	0.300	0.00
Model 1	Λ CDM, $\omega_{DE} = 0.1594$ ($h = 0.55$)	90.6	1.760	0.859	0.480	0.248	0.00
Model 2	Λ CDM, $\omega_{DE} = 0.4811$ ($h = 0.79$)	107.1	2.230	1.137	0.659	0.352	0.00
Model 3	w CDM, $w_0 = -0.85$	103.4	2.100	1.044	0.590	0.307	0.00
Model 4	w CDM, $w_0 = -1.15$	95.9	1.922	0.964	0.553	0.293	0.00
Model 5	$w_0 w_\alpha$ CDM, $w_\alpha = -0.2$	97.7	1.972	0.990	0.566	0.299	0.00
Model 6	$w_0 w_\alpha$ CDM, $w_\alpha = 0.2$	100.7	2.031	1.011	0.574	0.301	0.00
Model 7	Non-flat Λ CDM, $\Omega_K = -0.05$ ($\omega_{DE} = 0.3283$)	94.3	1.937	0.978	0.561	0.297	0.00
Model 8	EdS model, $\omega_{DE} = 0.0$ ($h = 0.38$)	78.0	1.402	0.651	0.349	0.174	0.00

Table 2. Details of the Aletheia simulations. Model 0 adopts a Λ CDM model with the cosmological parameters given in Table 1. All remaining models are obtained from model 0 by varying one evolution parameter as described in the definition in the second column. The parameters in parentheses represent the values of h or ω_{DE} adopted to compensate for a change in a density parameter. The remaining columns list the redshift of the initial conditions and of the five snapshots obtained at the given values of σ_{12} .

approximation of \mathbf{v} . We assume that the velocity field is constant inside each Voronoi cell² of the particles in the simulation. With this piece-wise approximation, the field is discontinuous at the edges of each cell and some small-scale information is lost. However, we propose a Monte-Carlo variation of this Voronoi method that compensates a small loss in accuracy by considerably reducing the number of calculations needed. This approach can be implemented without calculating the full Voronoi tessellation of our simulations. We simply populate the boxes with points sampled from a distribution that evenly covers the volume (in our case, a glass-like distribution, see below), and assign to each of them the velocity of the closest N-body particle. This results in a new particle distribution that reproduces our piece-wise approximation of the velocity field. The now evenly distributed samples can be used to estimate the smoothed velocity field by means of commonly used mass assignment schemes. Hereafter, we refer to this approach as the Monte-Carlo Voronoi method (MC-Voronoi).

In our implementation, we start by populating the simulation box with a sample of particles following a glass-like distribution generated using the recipe of Dávila-Kurbán et al. (2021). These samples provide a more homogeneous covering of the volume than a Poisson distribution with the same number of points, reducing the shot-noise contribution in our estimates. Each point in this distribution is assigned a velocity matching that of its closest neighbour among the simulation particles. We then use this new set of points to compute the CIC smoothed velocity field, $\bar{\mathbf{v}}$, on a regular mesh

$$\bar{\mathbf{v}}_i = \frac{\sum_j w(\mathbf{x}_i, \mathbf{x}_j) \mathbf{v}_j}{\sum_j w(\mathbf{x}_i, \mathbf{x}_j)}, \quad (17)$$

where $w(\mathbf{x}_i, \mathbf{x}_j)$ represents the CIC kernel evaluated at the positions of the node i of the grid and point j in the glass-like distribution. Note that, in contrast with directly applying a CIC assignment scheme to the N-body particles, in this case, our tracers sample the simulation box uniformly, and the velocity field thus obtained is not weighted by the density field; moreover, this method does not leave empty cells as long as the density of glass particles is high enough compared to the chosen grid size.

Other than the choice of the mass-assignment scheme, the other two important parameters in this procedure are the size of the grid

and the number of glass-like points used to sample the simulation volume. In this work, we adopt 1024^3 grid points to resolve the scales we are interested in. To save computation time (which grows linearly with the number of points in the sample), we only employed the same number of glass points as of particles in the simulation. Increasing this number can improve the accuracy of this method; however, our tests have shown that the gain is minimal in our case.

Once the velocity field has been computed on a regular grid, it can be used to estimate various statistics. In this work, we are interested in the velocity divergence auto power spectrum and its cross-power spectrum with the density field. We also use the CIC assignment scheme to reconstruct the density field on the same grid of 1024^3 points. We evaluated a second mesh grid shifted by half a grid size for each snapshot to correct for aliasing through an interlacing technique (Sefusatti et al. 2016). For calculating the power spectra, we used the publicly available library Pylians³ (Villaescusa-Navarro 2018), which Fourier-transforms the velocity field, obtains $\theta_{\mathbf{k}}$ in Fourier space, and uses it to calculate $P_{\theta\theta}(k)$ and $P_{\delta\theta}(k)$.

Although more accurate methods for estimating the smoothed velocity field exist in the literature, we chose this procedure due to its computational simplicity. Since we are interested in differences and ratios between power spectra rather than their absolute values, the MC-Voronoi method employed in this work is enough to reach solid conclusions. In particular, we performed preliminary tests comparing our results with the method proposed in Bel et al. (2019), which employs a Delaunay field estimator and found perfectly compatible outcomes. We leave a detailed comparison between these different methods for future work (Esposito et al., in prep).

5 RESULTS

In this section, we present the power spectra estimated with the technique described in Section 4. Fig. 1 shows the $P_{\theta\theta}(k)$ and $P_{\delta\theta}(k)$ estimated from the Aletheia simulations in the left and right panels, respectively. The solid lines correspond to the results for the cosmologies described in Table 2, while the dashed lines indicate the linear theory predictions. As expected, given that the snapshots of the different cosmologies correspond to the same values of σ_{12} , all models have the same power spectra at large scales but present some small deviations at small scales where the evolution mapping relation

² In a Voronoi tessellation, space is divided into regions around a set of particles such that each region contains all the points closer to its corresponding particle than to any other, forming a set of convex polyhedra.

³ <https://pylians3.readthedocs.io/en/master/>

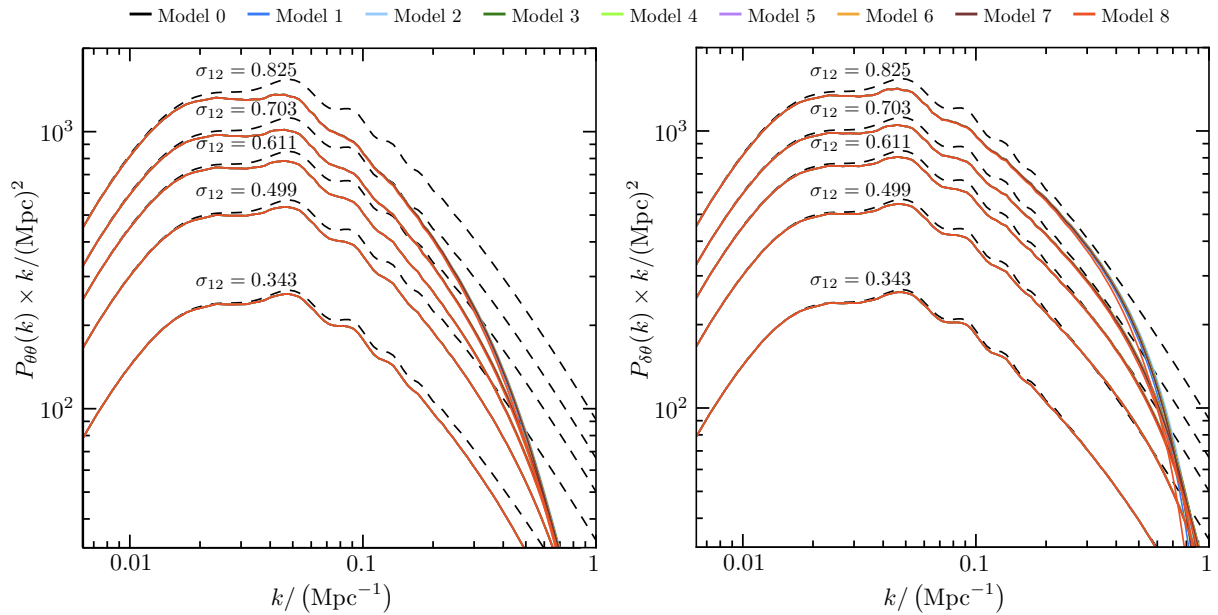


Figure 1. Velocity divergence auto- (left panel) and cross- (right panel) power spectra measured from the Aletheia simulations. The power spectra are multiplied by k for a clearer display of the lines. Each colour indicates a different cosmology for which the power spectra from all 5 snapshots are shown. Rather than being at the same z , each snapshot is extracted at the z at which each model reaches a given σ_{12} (indicated above each set of lines).

becomes approximate. The measurements of $P_{\delta\theta}(k)$ show a steep drop and a change of sign (which is not visible in the figure) that correspond to the appearance of vorticity. While the velocity field has no vorticity at the linear level, it is produced by the non-linear evolution of the density fluctuations (Pueblas & Scoccimarro 2009; Hahn et al. 2015). Such vorticity disrupts the cosmic flow and breaks the tight correlation between the density and velocity fields. Hence, vorticity causes the cross-power spectrum to drop at the scales when it becomes important and then change its sign at the scale of shell crossing.

The left panel of Fig. 2 shows the ratios of the measurements of $P_{\theta\theta}(k)$ in the different models to the one measured in the reference Λ CDM cosmology (model 0). The different panels correspond to our five reference values of σ_{12} increasing from bottom to top and the colour-coding matches that of Fig. 1. The deviations from model 0 become more significant with increasing σ_{12} , corresponding to increasing levels of non-linearities. Going from larger to smaller scales, we can identify different regimes when comparing the different models to our reference one: (1) at large linear scales, the $P_{\theta\theta}$ are almost undistinguishable because they share the same linear theory power spectra; (2) going to smaller scales, evolution mapping breaks down, and the different growth histories cause the power spectra to diverge from each other in the same direction as the $P_{\delta\delta}(k)$ do; (3) with the appearance of vorticity and as more particles shell-cross, the sign of the correlation between θ and δ changes (Hahn et al. 2015) and thus, the trend in the deviations between the different models is reverted and grows in the opposite direction. The maximum deviations in the range of scales that can be measured from these simulations go from less than 0.5 per cent at $\sigma_{12} = 0.343$ to approximately 5 per cent at $\sigma_{12} = 0.825$. The exception is model 8, which reaches 10 per cent deviations. This last case corresponds to an EdS cosmology with an extreme value for $h = 0.378$ and thus exhibits much larger deviations than the other models.

As shown by Sánchez et al. (2022), the differences in the matter power spectra of these models are related to their different structure-

formation histories, which can be described by the differences in the growth suppression factors $g(\sigma_{12})$ and its derivative $g'(\sigma_{12})$. We show here that this is also valid for velocity statistics and that we can use equation (10) not only for predicting $P_{\delta\delta}(k)$, but also $P_{\delta\theta}(k)$ and $P_{\theta\theta}(k)$ based on the results of our reference Λ CDM model.

We estimated the derivatives in equation (10) by assuming that this relation is exact for models 1 and 7 and solving the system of equations for $\partial P(k)/\partial g$ and $\partial P(k)/\partial g'$. We used equation (10) to approximate the measurements of $P_{\theta\theta}(k)$ of the remaining models.

The right panel of Fig. 2 shows the ratios of the $P_{\theta\theta}(k)$ measured from the simulations to the ones estimated using this recipe⁴. To simplify the comparison with the original model differences, the ranges of both axes are the same as those of the left panel. Equation (10) can indeed capture the differences between model 0 and the other cosmologies. The maximum residual differences range from approximately 0.1 per cent at $\sigma_{12} = 0.343$ to per cent level deviations at $\sigma_{12} = 0.825$. The $P_{\theta\theta}(k)$ of the EdS cosmology (model 8), which in the left panel shows the largest differences, is also recovered with the same level of accuracy as the other models.

Fig. 3 shows the result of the same procedure applied to $P_{\delta\theta}(k)$. The left panels show the differences between $k \times P_{\delta\theta}$ measured from the simulations and the one of model 0. The right panels show the differences between the same measurements and the predictions obtained using the ansatz of equation (10). As mentioned before, the non-linear $P_{\delta\theta}$ crosses zero at the scale of shell crossing at which the correlation between the density and velocity fields changes sign. This scale is reached by our measurements for some of the snapshots. Hence, we decided to show absolute differences in this case instead of relative differences, which are undefined at the zero-crossing. In order to discuss these results similarly to the ones presented in Fig. 2, we include in each panel a shaded region that includes values within ± 1 per cent of $k \times P_{\delta\theta}$ of model 0. We also notice in this case that

⁴ To see the results for the $P_{\delta\delta}(k)$, check Sánchez et al. (2022)

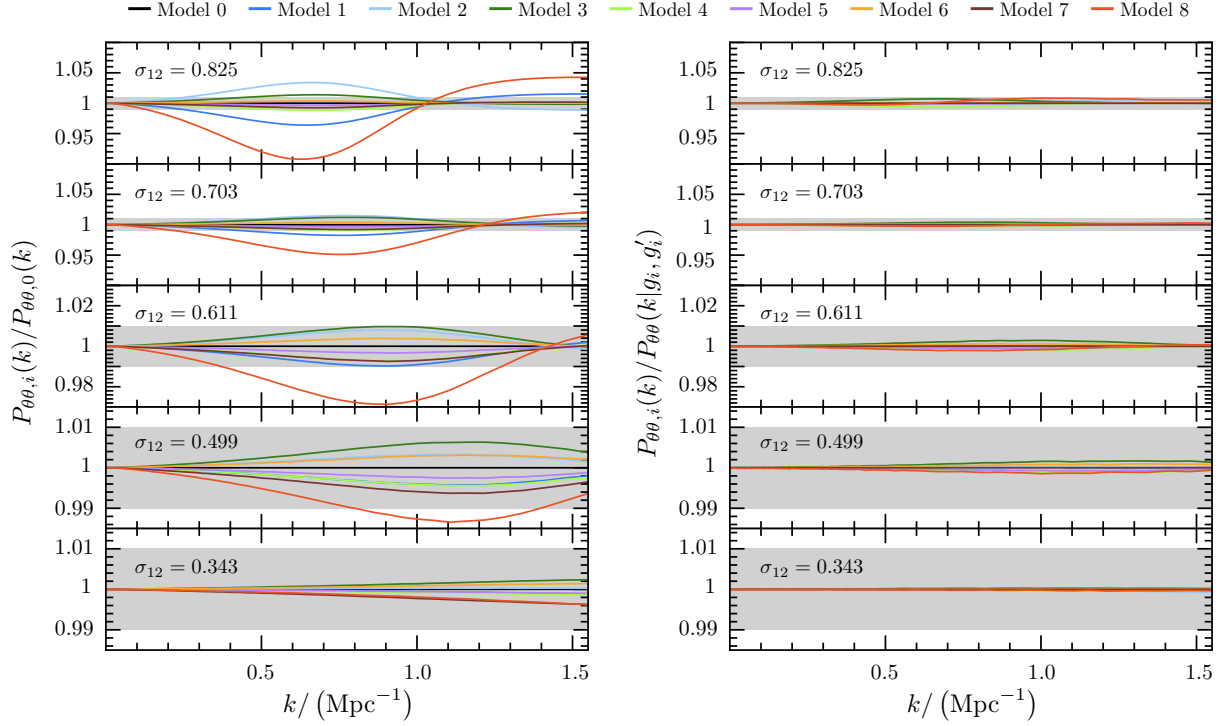


Figure 2. Ratios of velocity divergence auto-power spectra measured from the Aletheia simulations to that of model 0 (left panel) and to the predictions of equation (10) (right panel). The different colours correspond to different cosmologies described in Table 2. From bottom to top, the panels show the five snapshots extracted from the simulations at increasing values of σ_{12} . The shaded grey regions show 1 per cent deviations from model 0.

the lines leave the 1 per cent region as we move to smaller scales (larger values of k) and larger clustering (larger values of σ_{12}).

The right panel of Fig. 3 shows how equation (10) can predict also $P_{\delta\theta}(k)$ with high accuracy, with differences with the measured power spectra that are reduced well within the grey shaded regions. Note that equation (10) does not include ratios of power spectra, and it is thus well-defined at all scales. However, it is more difficult to give a meaningful estimate of the (relative) error that one would make when using equation (10) to predict the power spectra of the other models.

There is a deep connection between the evolution mapping approach and the cosmology-rescaling method proposed by Angulo & White (2010), which adapts a cosmological simulation to match a different target cosmology. When the cosmologies share the same shape parameters, this rescaling involves identifying the redshift at which the amplitude of the linearly-evolved matter density fluctuations (i.e., the value of σ_{12}) in the target cosmology matches that of the original cosmology. At this point, velocities are rescaled by the ratio of the factors $af(a)H(a)$ appearing in the continuity equation, aligning with the methodology employed in our work. The correction for differences in the growth histories in terms of $g(\sigma_{12})$, as given in equation (10), is analogous to the rescaling of the concentration-mass relation proposed by (Contreras et al. 2020). The simulation rescaling method has demonstrated practical success in various studies (e.g., Angulo & White 2010; Angulo et al. 2021; Ruiz et al. 2011; Zennaro et al. 2023). Our evolution mapping framework can be seen as a theoretical basis for why this approach works. Specifically, the spatial and temporal scaling that best matches the shape and amplitude of the linear power spectra between the two cosmologies also results in a good agreement of the full non-linear structure formation.

Our results show that the mapping of equation (10) indeed applies

also to the velocity field and, therefore, describes the full particle trajectories. Thus, any other statistic extracted from N-body simulations would follow, to some extent, the evolution mapping relation of equation (9).

By adopting physical density parameters and absolute Mpc units, we can take advantage of the evolution-mapping degeneracy in the cosmological parameters. This is useful for increasing the accuracy and performance of emulators and fitting functions, but most importantly, it simplifies our understanding of structure formation. This is yet another reason for avoiding the use of the traditional Hubble units, which obscure the impact of the different cosmological parameters on the evolution of cosmic structure.

6 CONCLUSIONS

We followed the approach of evolution mapping proposed in Sánchez et al. (2022) and applied it to velocity statistics. In particular, we employed a suite of dark matter only N-body simulations that share the same shape parameters (which determine the shape of $P_L(k, z)$), but cover a wide range of evolution parameter values (which determine the redshift evolution of the amplitude of $P_L(k, z)$) to show how—when evaluated at the same σ_{12} —the statistics of the velocity field, namely $P_{\theta\theta}(k)$ and $P_{\delta\theta}(k)$, are remarkably similar up to few percent differences at non-linear scales. The deviations appearing at smaller scales are due to the different growth histories that these models experience. Thus, we showed how modelling these deviations in terms of g and g' , can predict the $P_{\theta\theta}(k)$ and $P_{\delta\theta}(k)$ of a given model with sub-percent to percent level accuracy.

Measuring the smoothed velocity field using simulation particles as tracers is a challenging task, due to the lack of information in

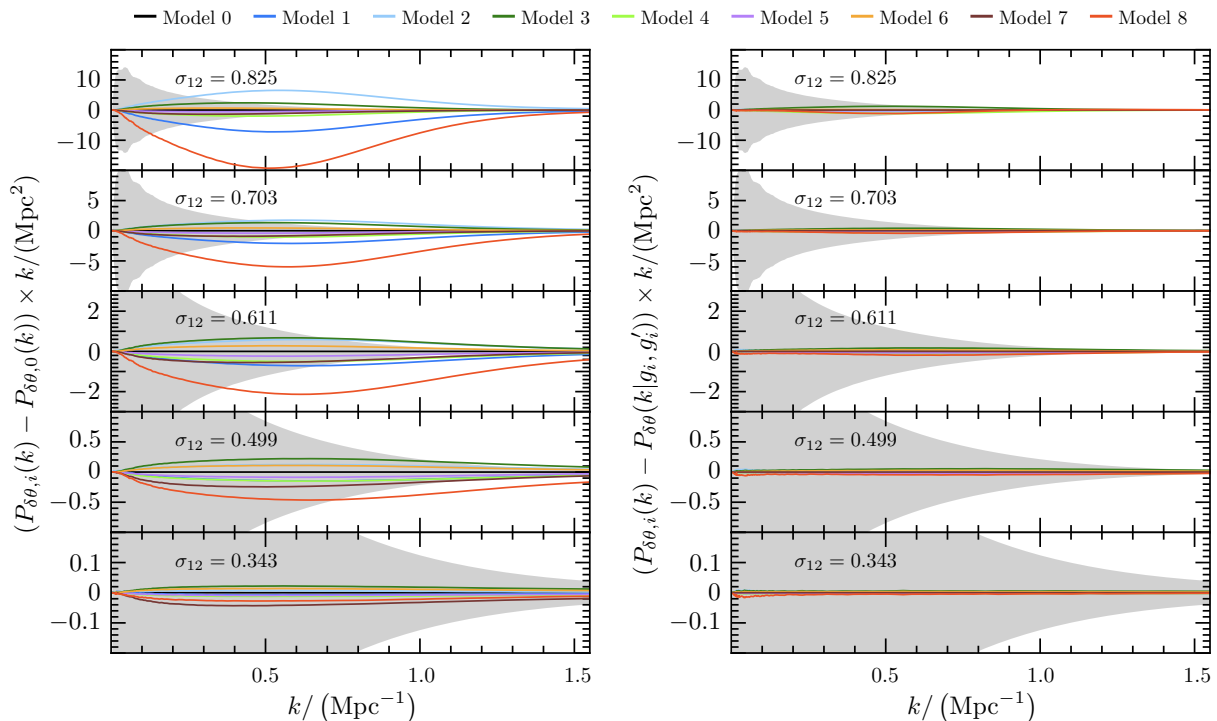


Figure 3. Differences of cross-power spectra of the velocity divergence with the density field measured from the Aletheia simulations with respect to model 0 (left panel) and to the predictions of equation (10) (right panel). The power spectra are multiplied by k for a clearer display of the lines. The different colours correspond to different cosmologies. From bottom to top, the panels show the five snapshots extracted from the simulations at increasing values of σ_{12} . The shaded grey regions show values within ± 1 per cent of the power spectra of model 0.

underdense regions. In this work, we adopted a new approach for estimating the velocity field on a grid through a Monte-Carlo sampling of the field under the assumption of a piece-wise constant approximation in the cells of a Voronoi tessellation. Given that a comparison of the power spectra of our different cosmologies shows little sensitivity to the specific method adopted, to infer them, we leave more detailed tests and comparisons of this and other methods for future works (Esposito et al., in preparation).

We highlight a limitation in GADGET-4 when performing velocity-related analyses with simulation snapshots that require a specific redshift. The `OUTPUT_NONSYNCHRONIZED_ALLOWED` option, while providing accurate particle positions at exact redshifts, leads to inconsistencies in velocities because particles are not synchronized in time, introducing potential biases that are difficult to predict. We thus recommend using a *start-stop* method instead, which we discuss in more detail in Appendix A where we address the problem.

As discussed in Sánchez et al. (2022), evolution mapping can streamline the design of emulators for the non-linear power spectrum and other density field statistics by reducing the number of required simulation nodes and redshift outputs, thus lowering computational demands. Traditional emulators often struggle with high-dimensional cosmological parameter spaces and assume restrictive parameter ranges. Evolution mapping simplifies this process by using a reference set of fixed evolution parameters and sampling over the parameter space defined by shape parameters and σ_{12} . Each node in this space corresponds to a simulation at a single redshift where the desired σ_{12} is achieved. The emulator’s predictions can then be adapted to any desired cosmology using the recipe in equation (10). This approach not only reduces the dimensionality of the parameter space but also enhances prediction accuracy. Our results indicate that the same method can be extended to build emulators for non-linear

velocity field statistics and the impact of redshift-space distortions on other clustering statistics. This extension further broadens the applicability of evolution mapping, making it a versatile tool for constructing comprehensive models of cosmological observations.

By adopting physical density parameters and absolute Mpc units, we can exploit the evolution- mapping degeneracy in cosmological parameters more effectively. This approach not only enhances the accuracy and performance of emulators and fitting functions but also significantly simplifies our understanding of structure formation. Using Mpc units avoids the complications associated with traditional Hubble units, which obscure the impact of different cosmological parameters on the evolution of cosmic structures. This clarity provides a compelling reason to standardize measurements in absolute units, simplifying the interpretation of cosmological analyses.

ACKNOWLEDGEMENTS

We would like to thank Raul Angulo and the BACCO project for providing useful scripts for benchmarking the codes used in this work. We also would like to thank Sofia Contarini, Carlos Correa, Andrea Fiorilli, Luca Fiorino, Nelson Padilla, Alejandro Perez, Andrea Pezzotta, Agne Semenaite and Matteo Zennaro for their help and useful discussions. This work was funded by the Deutsche Forschungsgemeinschaft (DFG, German Research Foundation) under Germany’s Excellence Strategy – EXC 2094 – 390783311. The Aletheia simulations were carried out and post-processed on the HPC system Cobra of the Max Planck Computing and Data Facility (MPCDF) in Garching, Germany. We acknowledge support from the European Research Executive Agency HORIZON-MSCA-2021-SE-01 Research

and Innovation programme under the Marie Skłodowska-Curie grant agreement number 101086388 (LACEGAL).

DATA AVAILABILITY

The data underlying this article will be shared with the corresponding author at a reasonable request.

REFERENCES

- Alam S., et al., 2017, *MNRAS*, **470**, 2617
- Alam S., et al., 2021, *Phys. Rev. D*, **103**, 083533
- Angulo R. E., Pontzen A., 2016, *Monthly Notices of the Royal Astronomical Society: Letters*, **462**, L1
- Angulo R. E., White S. D. M., 2010, *Monthly Notices of the Royal Astronomical Society*
- Angulo R. E., Zennaro M., Contreras S., Aricò G., Pellejero-Ibañez M., Stücker J., 2021, *MNRAS*, **507**, 5869
- Bel J., Pezzotta A., Carbone C., Sefusatti E., Guzzo L., 2019, *Astronomy & Astrophysics*, **622**, A109
- Bernardeau F., van de Weygaert R., 1996, *Monthly Notices of the Royal Astronomical Society*, **279**, 693–711
- Bernardeau F., van de Weygaert R., Hivon E., Bouchet F. R., 1997, *MNRAS*, **290**, 566
- Cautun M. C., van de Weygaert R., 2011, *arXiv e-prints*, p. arXiv:1105.0370
- Chevallier M., Polarski D., 2001, *International Journal of Modern Physics D*, **10**, 213
- Cole S., et al., 2005, *MNRAS*, **362**, 505
- Contreras S., Angulo R. E., Zennaro M., Aricò G., Pellejero-Ibañez M., 2020, *MNRAS*, **499**, 4905
- Crocce M., Pueblas S., Scoccimarro R., 2006, *Monthly Notices of the Royal Astronomical Society*, **373**, 369
- DESI Collaboration et al., 2024, *arXiv e-prints*, p. arXiv:2404.03002
- Dávila-Kurbán F., Sánchez A. G., Lares M., Ruiz A. N., 2021, *MNRAS*, **506**, 4667
- Efstathiou G., Davis M., White S. D. M., Frenk C. S., 1985, *ApJS*, **57**, 241
- Efstathiou G., et al., 2002, *MNRAS*, **330**, L29
- Eisenstein D. J., et al., 2005, *ApJ*, **633**, 560
- Feldbrugge J., 2024, Phase-Space Delaunay Tessellation Field Estimator (*arXiv:2402.16234*)
- Garny M., Taule P., 2021, *J. Cosmology Astropart. Phys.*, **2021**, 020
- Garrison L. H., Eisenstein D. J., Pinto P. A., 2019, *MNRAS*, **485**, 3370
- Guzzo L., et al., 2008, *Nature*, **451**, 541
- Hahn O., Angulo R. E., Abel T., 2015, *Monthly Notices of the Royal Astronomical Society*, **454**, 3920–3937
- Jennings E., 2012, *MNRAS*, **427**, L25
- Jennings E., Baugh C. M., Pascoli S., 2011, *MNRAS*, **410**, 2081
- Jennings E., Baugh C. M., Hatt D., 2015, *MNRAS*, **446**, 793
- Juszkiewicz R., Weinberg D. H., Amsterdamski P., Chodorowski M., Bouchet F., 1995, *ApJ*, **442**, 39
- Kaiser N., 1987, *MNRAS*, **227**, 1
- Koda J., et al., 2014, *MNRAS*, **445**, 4267
- Kravtsov A. V., Klypin A. A., Khokhlov A. M., 1997, *ApJS*, **111**, 73
- Linder E. V., 2003, *Phys. Rev. Lett.*, **90**, 091301
- Mo H., van den Bosch F. C., White S., 2010, *Galaxy Formation and Evolution*. Cambridge University Press
- Nusser A., Colberg J. M., 1998, *Monthly Notices of the Royal Astronomical Society*, **294**, 457
- Peebles P. J. E., 1980, *The large-scale structure of the universe*
- Potter D., Stadel J., Teyssier R., 2017, *Computational Astrophysics and Cosmology*, **4**, 2
- Pueblas S., Scoccimarro R., 2009, *Phys. Rev. D*, **80**, 043504
- Romano-Díaz E., van de Weygaert R., 2007, *MNRAS*, **382**, 2
- Ruiz A. N., Padilla N. D., Domínguez M. J., Cora S. A., 2011, *MNRAS*, **418**, 2422
- Sánchez A. G., 2020, *Phys. Rev. D*, **102**, 123511
- Sánchez A. G., Ruiz A. N., Jara J. G., Padilla N. D., 2022, *MNRAS*, **514**, 5673
- Schaap W. E., van de Weygaert R., 2000, *A&A*, **363**, L29
- Scoccimarro R., 2004, *Physical Review D*, **70**
- Sefusatti E., Crocce M., Scoccimarro R., Couchman H. M. P., 2016, *MNRAS*, **460**, 3624
- Springel V., 2005, *Monthly Notices of the Royal Astronomical Society*, **364**, 1105
- Springel V., Pakmor R., Zier O., Reinecke M., 2021, *MNRAS*, **506**, 2871
- Takahashi R., 2008, *Progress of Theoretical Physics*, **120**, 549
- Taruya A., 2016, *Phys. Rev. D*, **94**, 023504
- Teyssier R., 2002, *A&A*, **385**, 337
- Villaescusa-Navarro F., 2018, Pylians: Python libraries for the analysis of numerical simulations, Astrophysics Source Code Library, record ascl:1811.008 (ascl:1811.008)
- Yu Y., Zhang J., Jing Y., Zhang P., 2015, *Phys. Rev. D*, **92**, 083527
- Zennaro M., Angulo R. E., Pellejero-Ibañez M., Stücker J., Contreras S., Aricò G., 2023, *MNRAS*, **524**, 2407
- Zhang P., Zheng Y., Jing Y., 2015, *Phys. Rev. D*, **91**, 043522
- Zheng Y., Zhang P., Jing Y., Lin W., Pan J., 2013, *Phys. Rev. D*, **88**, 103510
- Zheng Y., Zhang P., Jing Y., 2015, *Phys. Rev. D*, **91**, 043523
- van de Weygaert R., Bernardeau F., 1998, in Mueller V., Gottloeber S., Muecket J. P., Wambsganss J., eds, *Large Scale Structure: Tracks and Traces*. pp 207–216 (*arXiv:astro-ph/9803143*)

APPENDIX A: PROBLEMS WITH NON-SYNCHRONIZED OUTPUTS IN GADGET4

In this appendix, we show how non-synchronized velocities can bias the velocity statistics in Gadget simulations in a way which is difficult to predict. To integrate particle trajectories most efficiently, GADGET (in all its versions) employs an adaptive time step scheme. In this way, particles in dense regions have smaller time steps than those in voids. The code can thus accurately integrate complicated trajectories for the former without wasting time with multiple time steps for straight trajectories of the latter. This implies that particles might be non-synchronised at a given time in the simulations, i.e. the equation of motions of different particles has been integrated up to different times. However, the time domain decomposition in GADGET ensures that, through their evolution, particles get synchronized at the so-called *synchronization points*. Since this set of points is discrete, the user will often request snapshots at redshifts at which particles are not fully synchronized.

The default option in GADGET-4 for these scenarios is to output a snapshot at the closest *synchronization point*. This can ensure that the output is fully consistent at the cost of small perturbations in the redshift of the output. This approach works in most scenarios but becomes problematic when the user needs a snapshot at a specific redshift. This can be the case, for example, when the user is comparing different cosmologies at the exact same redshift. Or, in the case of the Aletheia simulations, at the exact same σ_{12} .

One possible way to overcome this problem is to use the compile-time option `OUTPUT_NONSYNCHRONIZED_ALLOWED` (hereafter ONSA). In this case, when the code reaches the time of a requested snapshot, it linearly interpolates the particle positions to the given time (i.e. it does a final drift) by using the lastly updated velocities while leaving the latter untouched. This solution is exact in predicting the particle positions. Still, it introduces an unpredictable error in the velocities: the snapshot will contain velocities that not only are not at the requested redshift but not even all at the same redshift. The user can, in principle, overcome this problem by reducing

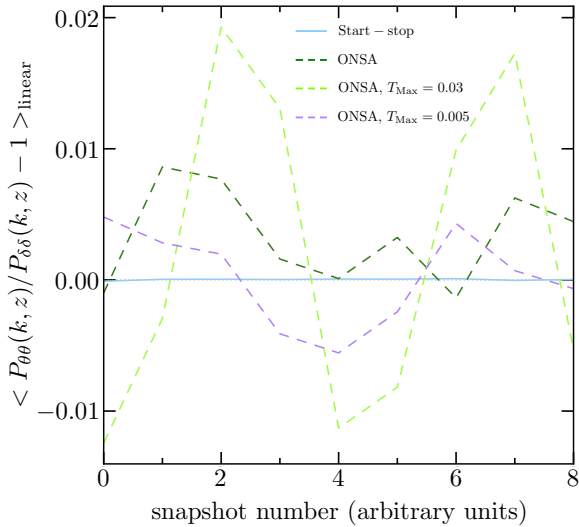


Figure A1. Relative differences in the amplitude of $P_{\theta\theta}$ and $P_{\delta\delta}$ across the simulation snapshots. The ratios between power spectra are calculated as the mean of $P_{\theta\theta}/P_{\delta\delta}$ in the first 8 bins of the measurements. The solid line represents the results obtained with the start-stop method, while the dashed lines are obtained using the ONSA flag. Where not indicated, the maximum allowed time step T_{Max} is the default one (0.01)

the largest time step allowed, but how effective this will be is difficult to estimate a priori.

We noticed this is the default behaviour of some versions of GADGET-3. Still, given that this version was never released publicly and branched into many versions, we refrain from making any tests with it in this paper. However, even though the effect is subtle and only affects velocities, we wish to make users who might overlook this issue consider it when using simulations for velocity statistics (e.g. analyses of velocity power spectra or redshift-space quantities).

As a quick solution that does not require code modifications, we employed a *start-stop* method in our simulations that we suggest applying when the user needs the output at a specific redshift. Given that the time domain decomposition is performed from the *TimeBegin* to the *TimeEnd* of the simulation, all the particles will be synchronized in all cases at these points. Hence, if the user performs the simulations until the first snapshot, then restarts from there until the second and so on, while each time changing *TimeBegin* and *TimeEnd*, this will ensure that all snapshots always have fully synchronized particles. The suggested approach for re-starting a simulation in GADGET-4 is using restart files. However, this approach is intended not to break the time integration scheme, saving the time domain decomposition calculated at the beginning of the simulation in the restart files. In this way, restarting a simulation at what was saved to be its end time will result in improper behaviour. As an alternative, we suggest saving the simulation snapshots in double precision when needed for a restart. This will ensure minimum information loss through the restarting of the simulation.

To show the effect of non-synchronized velocities, we performed a series of N-body simulations with different maximum allowed time steps. We employed the public versions of GADGET-4. All simulations include 512^3 dark matter particles in a $(2000 \text{ Mpc}/h)^3$ cubic volume. We perform each simulation in two ways: with the option of non-synchronized outputs and with the *start-stop* method. We estimate the error introduced in the velocity field (in particular in its divergence) by comparing $P_{\theta\theta}$ and $P_{\delta\delta}$ on linear scales; using non-synchronized velocities also changes the non-linear part of the $P_{\theta\theta}$, but here, we

focus our comparisons on scales for which we have solid theoretical predictions (see equation (15)). To obtain sensible results at these scales, we reduce the cosmic variance by starting our simulations from fixed-pair initial conditions at $z = 49$ with the 2LPTic code. We obtain 9 snapshots at $z = \{20, 15, 10, 8, 5, 4, 3, 2, 1\}$. We show in Fig. A1 the relative differences in the amplitude of the $P_{\theta\theta}$ and $P_{\delta\delta}$, estimated as the mean value of the power spectra in the first 8 bins. We present these measurements as a function of snapshot number to show how these deviations do not show any obvious correlation with redshift, being only determined by the choice of output redshift requested by the user. We present results for 3 different values of the maximum time step (T_{Max}) a particle may take (in $\ln(a)$): 0.01 (the default value), 0.03 and 0.005. We note that decreasing the maximum time step decreases the maximum error in the amplitude of $P_{\theta\theta}$. Nonetheless, the behaviour at a given snapshot is difficult to predict and reaching very high precision (like the one we needed for this work) would require very small T_{Max} , which largely increases the computation time. We thus encourage users who need accurate measurements of the velocity field to rather use the start-stop method suggested here (solid line in Fig. A1), which correctly captures the expected amplitude of $P_{\theta\theta}$.

This paper has been typeset from a $\text{\TeX}/\text{\LaTeX}$ file prepared by the author.